Analysis of Cracking Characteristics for Various Indenter Shapes using the Cohesive Zone Model

Hong Chul Hyun*, Felix Rickhey*, Jin Haeng Lee**, Minsoo Kim*, and Hyungyil Lee*

* Dept. of Mechanical Engineering, Sogang University, Seoul, S. Korea
** Division for Research Reactor, Korea Atomic Energy Research Institute, Daejeon, S. Korea

Abstract: During indentation of brittle materials, cracks may be forming around the impression, depending on load conditions, material and indenter geometry. We investigate the effect of indenter geometry (half-included angle, number of edges) on crack characteristics by indentation cracking test and finite element analysis (FEA). Considering conditions for crack initiation and propagation, an FE model is established featuring cohesive interfaces in zones of potential crack formation. After verification of the FE model through comparison with experimental results for Berkovich and Vickers indentations, we study the crack shapes for diverse indenter geometries in Abaqus and establish a relation between crack size and number of indenter edges. Based on this relation as well as the effect of indenter angle on crack size, a formula is established which enables us to predict from the crack size obtained with a reference indenter (such as Berkovich or Vickers) the crack size for an indenter of different geometry.

Keywords: Indentation Cracking Test; Brittle Materials; Cohesive Zone Model; Indenter Geometry; FEA

1. Introduction

For the past 30 years, abundant research has been conducted to extract the fracture toughness K_c from indentation tests. Effort has been put into finding a relation between K_c and the crack length c by transferring theory valid for single cracks to the more complex multi crack systems being generated during indentation. In contrast to traditional K_c evaluation methods, the fracture toughness can be readily obtained by only one indentation on a small specimen, making the method cost- and time-saving.

Based on Hill's expanding cavity model (Hill, 1950), Lawn et al. (1980) and Anstis et al. (1981) suggested a well-known equation to derive K_c from crack length c, indentation load $P_{\max}$, hardness H and Young's modulus E (Figure 1)

$$K_c = \alpha \left(\frac{E}{H}\right)^{1/2} \left(\frac{P}{c^{3/2}}\right) \quad (1)$$

For Vickers indentation on a number of glasses and ceramics, Anstis et al. (1981) found the indenter geometry factor α to be 0.016±0.004. Despite the advantage of Lawn et al.'s model – once α is known, K_c is calculated by values that can be readily obtained during indentation – Equation 1 contains several assumptions and simplifications. To date, no concrete method has been developed as to how to obtain α. On the other hand, the *in situ* observation of crack nucleation and growth, which may be taking place during loading and unloading, is difficult in real indentation. From the surface cracks alone, it is impossible to infer the whole crack system and methods such as focused ion beam (FIB) tomography are tedious and expensive. Since, depending on material properties and indenter shape, cracks may be simple radial surface cracks but also well-developed cracks (long, deep half-penny cracks), for an accurate evaluation of K_c a detailed investigation of the crack's subsurficial part and the coefficient α is required.

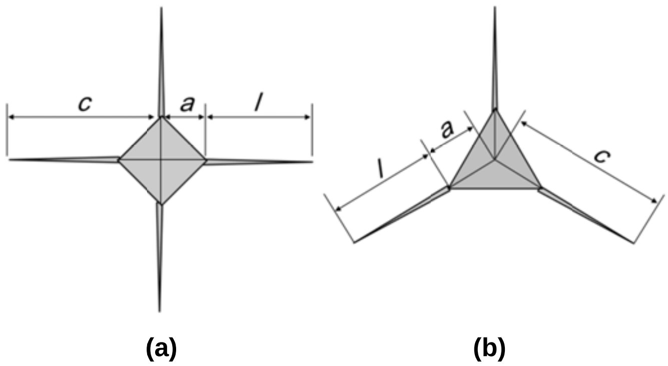

Figure 1. Schematic figure of cracking induced by (a) 4-sided and (b) 3-sided pyramidal indenter and (c) half-included angle ψ.

Dukino and Swain (Dukino, 1992) determined c for Vickers and Berkovich indentation for a number of materials and formulated a relation between c and number of cracks n_c based on Ouchterlony's (1976) study; yet it has not been expanded to general indenter geometries. Due to a number of reasons, the accuracy of fracture toughness values obtained by indentation is low. Ponton and Rawing (1989a,b) found that the application of most of the existing formulae resulted in a deviation of above 30 % from real K_c-values. Quin and Bradt (Quin, 2007) also compared K_c-values to real K_c-values and pointed out the limitations of Vickers indentation.

For further systematic investigation, other evaluation techniques such as FEA-based approaches have been developed (Zhang, 2001; Tang, 2008). Gao and Bower (2004) and Lee et al. (2012) proposed indentation crack analysis techniques using the cohesive zone model (CZM). The CZM simulates the atomic interaction potential by a simple traction separation law, thereby transferring nano-scale material behavior to the continuum scale. The CZM has proven useful when the plane of crack propagation can be anticipated. In this study, the effect of indenter geometry (half-included angle ψ and n_c) on crack characteristics is to be investigated for more general indenter shapes. Part 2 provides a description of indentation cracking analysis and the FE model featuring cohesive interfaces while in part 3, the crack analysis model is verified through comparison to test results obtained with Vickers indenters. In part 4, we compare crack lengths obtained by indentation on Si (100) and Ge (100) specimens with FE analysis results. After having ascertained the crack type, we investigate the relation between the number of indentation cracks and crack length.

2. Cohesive zone model and traction separation law

We apply the CZM to simulate crack nucleation and propagation in the material around the impression. Material damage is governed by an energy-based traction separation law (Figure 2). Accordingly, the cohesive traction T increases with separation δ up to the point where the separation between the two cohesive surfaces reaches a critical value (σ_{max}). Beyond σ_{max} the cohesive traction decreases monotonically to zero. Once the cohesive traction gets zero, the cohesive bond loses all its stiffness and an irreversible crack forms. The CZM is characterized by the shape of the traction separation curve and damage variables. However, in former studies (Hutchinson, 2000; Williams, 2002; Jin, 2005) it was found that the shape of the traction-separation curve does not influence the cracking behavior. We therefore assume the bilinear elastic traction separation law shown in Figure 2. In this case, three variables must be specified for a full description; the damage initiating stress σ_{max}, the corresponding displacement δ_{max} and the displacement leading to total failure, δ_c (or alternatively, the critical fracture energy Γ). The bilinear traction separation law can be expressed as

$$T = \begin{cases} \dfrac{\sigma_{max}}{\delta_{max}}\delta & \text{for } 0 \le \delta \le \delta_{max} \\ \dfrac{\sigma_{max}}{\delta_c - \delta_{max}}\left(\delta_c - \delta\right) & \text{for } \delta_{max} \le \delta \le \delta_c \end{cases} \tag{2}$$

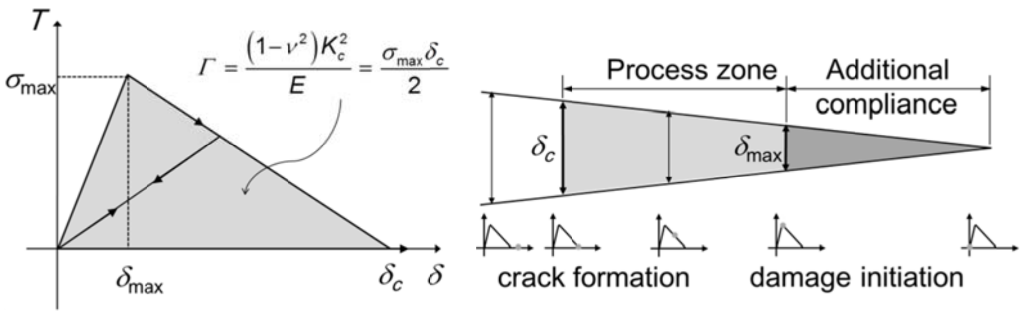

Figure 2. Bilinear traction-separation relation for cohesive zone model.

The fracture energy – the area under the traction separation curve of Figure 2 – is related to the fracture toughness through

$$\Gamma = \frac{K_c^2}{E'} = \frac{1}{2}\sigma_{max}\delta_c \quad ; \quad E' = \begin{cases} E & : \text{plane stress} \\ E/(1-\nu^2) & : \text{plane strain} \end{cases} \tag{3}$$

where ν is Poisson's ratio. Special-purpose cohesive elements (COH3D8 in Abaqus) of zero thickness are placed in the planes of potential crack propagation, and the traction separation law parameters are readily specified (Abaqus, 2010). Lee et al. (2012) came to the following conclusions: First, using a bilinear traction separation law the crack length c is independent of the ratio δ_{max}/δ_c; second, for well-developed cracks ($c>>a$), a change of minimum element size and σ_{max} (Γ= const.) does not exert significant influence on c; and third, to ensure crack propagation and to satisfy the linear elastic fracture condition ($c>>$process zone size), σ_{max} should be at least ~$0.2\sigma_o$ (σ_o: yield stress).

To study the change of crack size and shape with indentation variables (such as indentation depth h_t, P_{max}, ψ or n_c), the finite element analysis model shown in Figure 3 is used. The 3D 1/3 and 1/4 models (Figure 3a-c) consist of approximately 87,000 elements and 97,000 nodes; the full model is composed of approximately 260,000 elements and 270,000 nodes (Figure 3d).

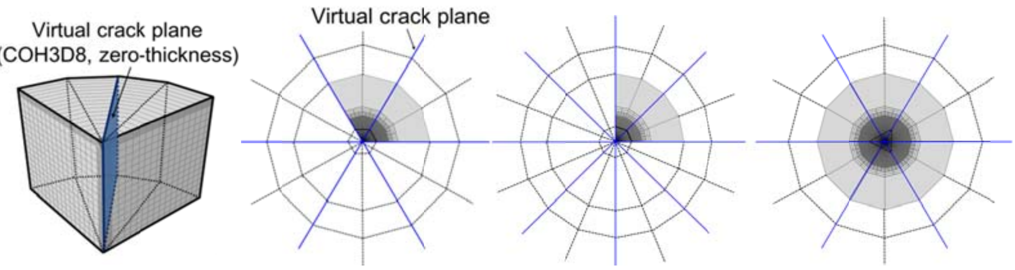

Figure 3. (a) 3D FE model for 4-sided indenter; (b) 1/3 model for 3- and 6-sided indenters; (c) 1/4 model for 8-sided indenters; (d) full model for 3-sided indenters

Owing to geometric symmetry, we have a purely mode I loading state so that only the normal traction separation law parameters are of concern. The stress state beneath the impression and consequently the crack length depend on the friction coefficient f. Since the friction coefficients of the materials used in this study range between 0.1~ 0.3, they are set to $f = 0.2$. The nodes lying on the axis of symmetry (z-axis, Figure 9) are restricted to movements in vertical direction (indentation direction). The bottom surface is fixed, and a diamond indenter ($E_I = 1016$ GPa, ν_I= 0.07) is pressed into the top surface (negative z-direction).

3. Cracking analysis for 4-sided indenters and comparison to experimental results

Material properties for the five materials used in this study (Si_3N_4 (NC132), glass ceramic, Si_3N_4 (NC350), aluminosilicate glass, soda-lime glass) are listed in Table 1. Values for E/H are taken from Anstis et al. (1981), values for Poisson's ratio from Lee et al. (2012). The yield stresses σ_o are obtained by trial and error. The crack lengths are recorded for different indentation loads in the range P_{max} = 1 ~ 100 N (Table 1). The maximum load value beyond which $P_{max}/c^{3/2}$ is constant varies with material. For Si_3N_4 (NC132), $P_{max}/c^{3/2}$ converges to a constant value beyond a relatively high load $P_{max} \geq 80$ N, whereas for aluminosilicate glass and soda-lime glass convergence is reached at much lower loads $P_{max} \leq 3$N (Figure 4). Similarly, the ratio c/a above which $P_{max}/c^{3/2}$ is constant is material-dependent. For aluminosilicate glass, soda-lime glass and glass ceramic, $P_{max}/c^{3/2}$ converges to a constant value at low ratios $c/a \leq 2.0$ (Figure 4). Generally, when E/H is small, well-developed cracks form even at low c/a ratios. For $c/a \geq 2.5$, the ratio $P_{max}/c^{3/2}$ attains a constant value and a semicircular crack forms, independent of the material. Results obtained by FEA and experiments are listed in Table 1. The experimental value for $P_{max}/c^{3/2}$ is calculated using Equation 1 with $\alpha = 0.016$ and the K_c values provided by Anstis (1981). For the case that well-developed cracks form, the FEA results for $P_{max}/c^{3/2}$ differ from the experimental values by 12 %. Considering the error associated with the crack length measurement, we may state that the cracking analysis using the CZM is relatively accurate for evaluating crack growth and shape. The impression and crack morphology obtained by experiment and FEA after indentation on Si_3N_4 (NC132) with P_{max} = 100 mN is depicted in Figure 5.

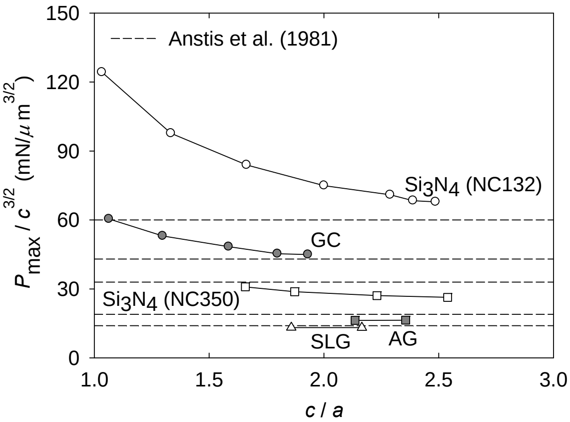

Figure 4. $P_{max}/c^{3/2}$ vs. c/a for 5 materials.

4. Cracking characteristics for diverse indenter shapes

4.1 Indentation cracking tests with 3-sided indenters

In contrast to Vickers indentation, 3-sided indenter induced cracks do not exhibit symmetry with respect to the plane normal to the cohesive plane and through the origin. The indenter shape is characterized by the number of indenter edges (equal to the number of developed cracks n_c) and the half-included angle ψ (Figure 1c). Si(100) and Ge(100) specimens are indented using the Nano Indenter-XP (Agilent Technologies). Radial crack length c and impression size a are measured for various ψ and P_{max} values and crack characteristics are compared with numerical analysis results. a is the radial distance from the center to the corner of the impression while c is the radial distance from the center to the crack's end (Figure 1b); the values for a and c in Table 2 are averaged values.

The half-included angles are $\psi = 35.3°$ (cube-corner), 45°, 55°, 65.3° (Berkovich). Load-controlled indentation is performed with loads up to $P_{max} = 50$ mN. Jang and Pharr (2008) showed that the loading rate v_i does not have influence on the crack length for v_i = 0.5 mN/s ~ 5.0 mN/s; the loading rate is set to 0.5 mN/s. Since Ge(100) has a comparatively low fracture toughness,

Table 1. Values for *c* from FE analysis and nano-indentation test.

Materials, K_c (MPa·m$^{1/2}$)	FE Analysis (σ_{max} = 0.5 GPa)					Indentation test [(1)]
	E/H[(1)]	σ_o[(2)] (GPa)	P_{max} (N)	c (μm)	$P/c^{3/2}$	$P/c^{3/2}$
Si_3N_4 (NC132), 4.0	300 / 18.5	10.2	5	12.1	124.2	60
			10	21.9	97.7	
			20	38.5	83.9	
			40	65.8	75.0	
			60	89.3	70.9	
			80	109.1	68.4	
			100	129.2	67.9	
Glass ceramic (C9606), 2.5	108 / 8.4	4.5	5	18.8	60.4	43
			10	32.9	53.1	
			20	55.5	48.3	
			40	91.9	45.3	
			50	107.1	45.0	
Si_3N_4 (NC350). 2.0	170 / 9.6	4.5	3	12.8	30.9	33
			5	16.7	28.8	
			10	23.2	27.1	
			20	32.9	26.3	
Aluminosilicate glass, 0.91	89 / 6.6	3.6	3	15.2	16.4	19
			5	19.3	16.3	
Soda lime glass, 0.74	70 / 5.5	3.1	1	9.6	13.2	14
			3	17.5	13.1	

(1) From Anstis (1981); (2) obtained by trial and error

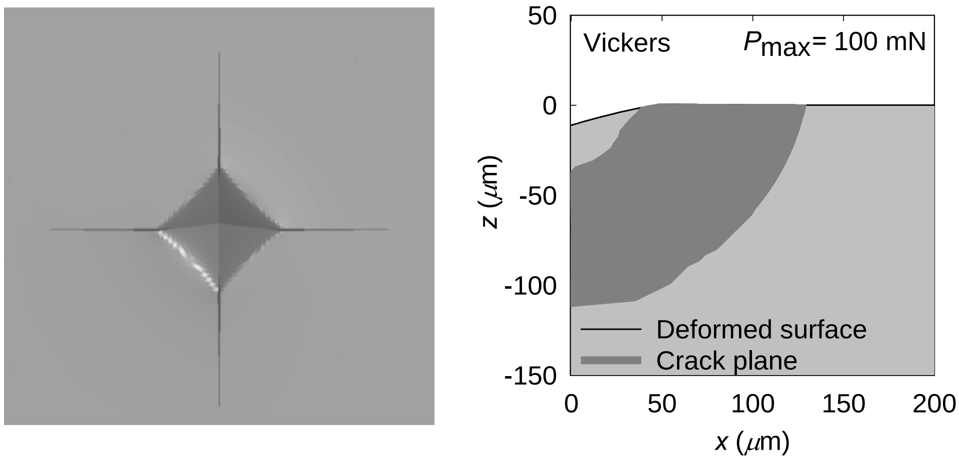

Figure 5. Crack morphology after unloading for Si_3N_4. *left*: experiment; *right*: FEA

considerable chipping is observed when using sharp indenters (ψ=35.3°, 45°) (Figure 6a). Data from indentation tests in which chipping occurred is excluded, so that only indenters with ψ = 35.3°, 45° [Si(100)] and ψ = 65.3° [Ge(100)] are used with loads P_{max} = 10, 20, 30, 75, 100mN. For each remaining combination of ψ and P_{max} 9 tests are conducted. Values for a and c are shown in Table 2. The differences between the crack lengths are below 5 %.

a is independent of ψ; yet, c increases with decreasing ψ. For equal loads (equal projected impression areas), the smaller ψ the higher is the indentation depth. As a result, the crack driving force increases and also c, as can be seen in Table 2. SEM images of the impression and the crack shape for the combination (P_{max} = 50 mN, ψ = 55°) are shown in Figure 6b and 6c. In both specimens, cracks have formed at all corners of the impression and have propagated in radial direction.

Table 2. *a* and *c* from nano-indentation test and FEA for Si(100) and Ge(100).

ψ (°)	Materials	K_c (MPa·m$^{1/2}$)	Nano-indentation test			FE Analysis	
			P (mN)	c (μm)	c/a	c (μm)	c/a
55	Si (100)	0.7	50	3.37	1.87	3.38	1.86
		1.0				2.56	1.29
	Ge (100)	0.6		4.82	2.50	3.84	1.94
		0.5				4.50	2.12
65.3	Si (100)	0.7	50	2.48	1.42	2.62	1.44
		1.0				-	-
	Ge (100)	0.6	50	3.63	1.87	3.03	1.43
			75	4.90	1.84	4.10	1.69
			100	5.96	2.02	4.99	1.73
		0.5	50	3.63	1.87	3.60	1.63

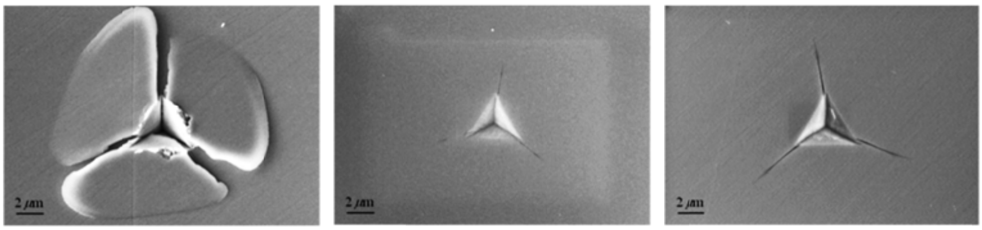

(a) (b) (c)

Figure 6. SEM images: (a) chipping in Ge(100) (ψ = 35.3°, P_{max} = 50 mN); impression and radial cracks in (b) Si(100), and (c) Ge(100) (ψ = 55°, P_{max} = 50 mN)

4.2 FE analysis with 3-sided indenters and comparison with experimental results

For the CZM-based indentation cracking analysis we have to specify values for the material properties K_c and Γ. In order to predict cracking behavior of real materials, the Young's modulus E and yield stress σ_o have to be determined accurately. E and H can be measured during the indentation test. Young's modulus can be obtained by the O-P (Oliver and Pharr) method (Oliver, 1992)

$$S = \left.\frac{dP}{dh_t}\right|_{h_t = h_{\max}} = \beta \frac{2}{\sqrt{\pi}} E_r \sqrt{A} \quad ; \quad \frac{1}{E_r} = \frac{\left(1-\nu^2\right)}{E} + \frac{\left(1-\nu_I^2\right)}{E_I} \tag{4}$$

where S, E_r and A are initial slope of the unloading curve, effective Young's modulus and impression size at $P_{\max}$, respectively. The geometric coefficient β is 1.034 for cube corner and Berkovich indenters. The test is repeated 9 times, with $P_{\max} = 50$ mN and $\psi = 65.3°$ (Berkovich). For indentation depths $\geq 0.15\,\mu$m, we obtain for Si(100) $\{H, E\} = \{12.0, 180\}$ and for Ge(100) $\{H, E\} = \{10.0, 144\}$ [GPa]. However, difficulties regarding the range of regression for acquiring S and the evaluation of the impression size A (contour is "blurred" due to sink-in/pile-up) may result in inaccurate values for E. The E value obtained by the O-P method is therefore taken as a start value in the FE analysis and modified until the $P{-}h_t$ curve matches the experimental one. Figure 7 shows the curves for Si (100), $P_{\max} = 50$ mN. When setting in FEA $\{E, \sigma_o\} = \{138, 5.4\}$ for Si(100) and $\{E, \sigma_o\} = \{113, 4.7\}$ [GPa] for Ge(100), we obtain, applying the O-P method, $\{H, E\} = \{12.0, 180.8\}$ and $\{H, E\} = \{10.2, 143.4\}$ [GPa], respectively, values that are close to the experimental ones.

3-sided indenters with $\psi = 55°$, 65.3° are employed in the analysis. The full model is used here. Indentations are performed with $P_{\max}$ = 50 mN. Fracture toughness values (Anstis, 1981; Jang, 2008) and crack lengths for diverse indentation loads are listed in Table 3. For $\psi = 55°$ and Si(100), the deviation between experimental and FEA crack lengths is about 1.4 % when assuming $K_c = 0.7$ MPa·m$^{1/2}$, and about 30 % when assuming $K_c = 1.0$ MPa·m$^{1/2}$. For $\psi = 65.3°$, the deviation is 5 % when assuming $K_c = 0.7$ MPa·m$^{1/2}$ (with $K_c = 1.0$ MPa·m$^{1/2}$ and $\psi = 65.3°$, no cracks formed). Thus, based on the FEA results, the fracture toughness of Si (100) is approximately $K_c = 0.7$MPa·m$^{1/2}$. For Ge(100), the deviation in crack lengths using indenters with $\psi = 55°$ and $\psi = 65.3°$ is 20 % and 16 %, respectively. When assuming $K_c = 0.5$ MPa·m$^{1/2}$, the deviation decreases to 6.6 % and 0.8 %, respectively.

4.3 Formation of cracks induced by 3-sided indenters

Due to geometric reasons, asymmetric cracks (i.e. not symmetric with respect to the plane normal to the cohesive interface and through the origin) may be induced by 3-sided indenters, as illustrated in Figure 9 (crack types 2 to 5). Figure 8 shows the shape of the crack in zone A obtained after Berkovich indentation ($\psi = 65.3°$) on an elastic-perfectly plastic material with $E = 200$ GPa, $\sigma_o = 5$ GPa, $\nu = 0.3$, $\sigma_{\max} = 0.5$ GPa, $\Gamma = 0.0025$ GPa·μm ($K_c = 0.74$ MPa·m$^{1/2}$). In zone A, a circular crack has formed after indentation to $h_{\max} = 1.0\,\mu$m and subsequent unloading, whereas in zone B, the indenter has not caused any cracking. The change in displacement δ (i.e. the distance between nodes that were initially at the same position) with indentation depth h_t is observed at the point $(x, z) = (0, -5.0)\,\mu$m (Figure 9) and depicted in Figure 10 (*left*). Here, the critical displacement is $\delta_c = 1.0\,\mu$m. Up to $h_t = 0.65\,\mu$m, δ increases uniformly in both zones, but for $h_t \geq 0.65\mu$m, δ rises sharply in zone A while it decreases to zero in zone B.

The half-included angle is now changed to $\psi = 55°$ and $\psi = 75°$ and again crack shape and length are determined for $h_{max} = 1.0\,\mu$m. For both ψ values, cracks are only generated in zone A. We increase the indentation depth to $h_{max} = 2.0\,\mu$m (Berkovich), but still cracks form only in zone A. The δ-h_t graphs corresponding to point $(x, z) = (0, -10)\,\mu$m is shown in Figure 10 (*right*). Up to h_t = 1.1 μm, curves for A and B increase in a similar manner, but afterwards δ increases further only in zone A. Using 3-sided indenters, the number of cracks is $n_c = 3$ for all indentation depths, and the crack shape corresponds to crack type 2 in Figure 9.

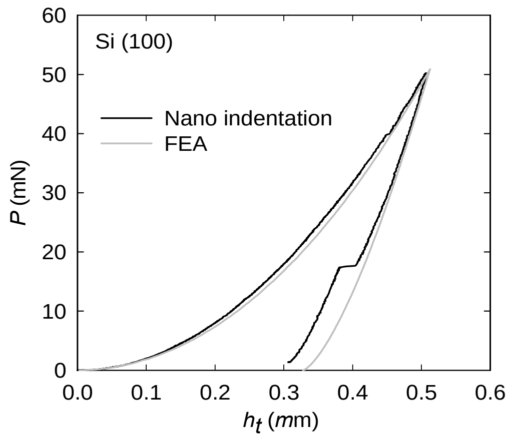

Figure 7. Indentation load-depth curves obtained from FE analysis and indentation test for Si(100).

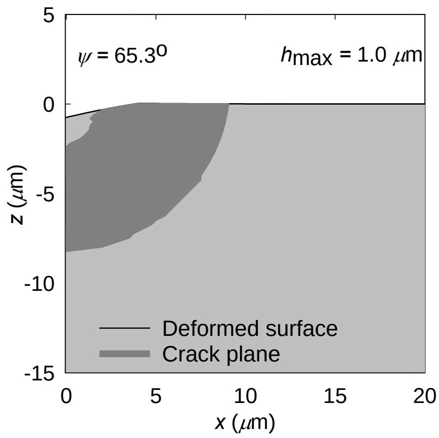

Figure 8. Deformed surface and crack shape at fully unloaded state for ψ = 65.3° & h_{max} = 1 μm.

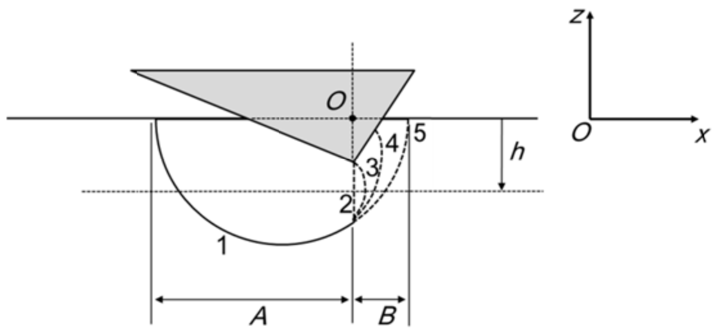

Figure 9. Possible types of cracks induced by a 3-sided pyramidal indenter (side-view).

Table 3. Variation of *c* and *a* with indentation variables (3-sided indenter).

E = 200 GPa, σ_o = 5 GPa, ν = 0.3, f = 0.2, K_{IC} = 0.74 MPa·m$^{1/2}$, δ_{max}/δ_c = 1/4				
Cohesive zone properties	ψ (°)	h_{max} (μm)	P_{max} (mN)	c (μm)
σ_{max} = 0.5 GPa Γ = 0.0025 GPa·μm	55	1.0	122.4	6.89
	65.3	1.0	237.3	9.06
		2.0	946.5	23.2
	75	1.0	524.4	11.9

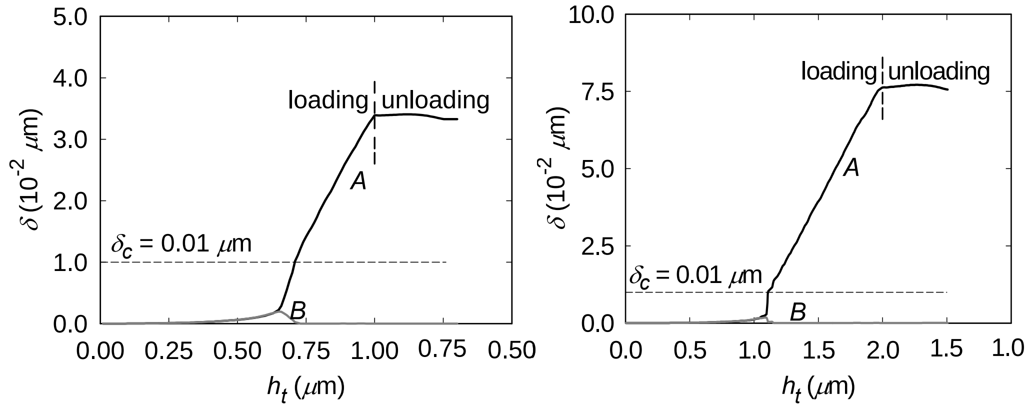

Figure 10. Separation vs. indentation depth. *left:* h_{max} = 1 μm; *right:* h_{max} = 2 μm.

4.4 Change of crack size with indenter shape

Ouchterlony (1976) established a relation between mode I stress intensity factor K and n_c

$$K = k_1(n_c)\ K_F; \quad k_1(n_c) = \sqrt{\frac{n_c}{2} / \left(1 + \frac{n_c}{2\pi}\sin\frac{2\pi}{n_c}\right)} \tag{5}$$

k_1 is the normalized stress intensity factor and $K_F = F/(\pi c)^{1/2}$ for a centrally loaded star crack, where F is the central expansion force (crack opening force). The following relations between K_c, P and c exist (Dukino, 1992)

$$K_c \propto x_B P / c^{3/2} \quad ; \quad K_c \propto x_V P / c^{3/2} \tag{6}$$

Here x_B (Berkovich) and x_V (Vickers) are indenter shape-dependent coefficients. They are related through

$$\frac{x_B}{x_V} = \frac{k_1(4)}{k_1(3)} \tag{7}$$

According to Equation 5, the ratio of k_1 for Vickers to k_1 for Berkovich is approximately 1.073. The crack length ratio (Vickers to Berkovich) is then $(1.073)^{2/3} \approx 1.05$. Equivalently, the ratios of crack length using Berkovich to crack length using 6-sided pyramid ($n_c = 6$), 8-sided pyramid ($n_c = 8$), 12-sided pyramid ($n_c = 12$) indenters are $(1.244)^{2/3} \approx 1.16$, $(1.327)^{2/3} \approx 1.21$, $(1.408)^{2/3} \approx 1.26$, respectively. Plotting the normalized crack length (i.e. normalized by the Vickers crack length c_V) versus n_c, we get the grey curve in Figure 11. As expected, c decreases to 0 for $n_c \to \infty$ so that cracks are supposed not to occur for spherical indenters.

To study the change of crack length with crack shape, analysis is performed with the FE models in Figure 3a-c. Material properties are $E = 200$ GPa, $\sigma_o = 5$ GPa, $\nu = 0.3$, $\sigma_{max} = 0.5$ GPa, $\Gamma = 0.0025$ GPa$\cdot\mu$m (or $K_c = 0.74$MPa$\cdot$m$^{1/2}$). Indenters with $\psi = 69.8°$ (8-sided pyramid), 69.4° (6-sided pyramid), 68° (Vickers), 65.3° (Berkovich) are employed. ψ is chosen such that projected impression areas are equal at equal loads. After indenting to $h_{max} = 0.4 – 1.2\ \mu$m and subsequent unloading, we measure c and a. Since the ratio c/a has a constant value independent of δ_{max} and (δ_{max}/δ_c) (Lee, 2012), we set $\delta_{max}/\delta_c = 1/4$. At equal maximum loads the radial length and depth of the crack increase with decreasing n_c (Figure 12, *left*). On the other hand, at equal indentation depths the Berkovich indentation load is larger than that for Vickers, 6-, and 8-sided pyramid indenters. This means, if one wants to accurately compare changes in crack length with indenter shape, one has to indent applying equal loads or one has to infer the crack length at an equal load value. It had been purported that only when well-developed cracks (half-penny crack, $c/a \geq 2.5$) form, c and $P_{max}^{2/3}$ were proportional to each other (Anstis, 1981; Niihara, 1983). However Jang and Pharr (2008) noticed recently that in Si(100) and Ge(100), the crack length was proportional to $P_{max}^{2/3}$ also at low loads, yet did not investigate a larger range of materials.

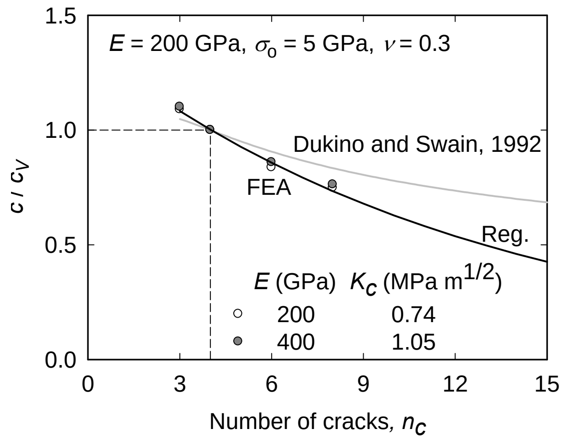

Figure 11. Normalized crack length c/c_V vs. n_c.

The maximum difference between $P_{max}/c^{3/2}$ values obtained for different indenter shapes at indentation depths h_{max} = 0.4 – 1.2 μm is 27 %, the average deviation is around 18 %. From this we conclude that $P_{max}/c^{3/2}$ is constant at low loads only for Si(100), Ge(100). For four types of indenters, $P_{max}/c^{3/2}$ converges to a constant value when $h_{max} \geq 0.8$ μm. The critical value for c/a (where $P_{max}/c^{3/2}$ converges to a constant value) increases with n_c (Figure 12, *right*). Under the condition that a well-developed crack has formed (i.e. $P_{max}/c^{3/2}$ = constant), the change of c with indenter geometry is analyzed. Applying the same load that was used in Vickers indentation, the crack lengths for Berkovich ($c_{B'}$), 6-sided pyramid ($c_{six'}$), and 8-sided pyramid indenter ($c_{eight'}$) are evaluated at $c_{B'}/c_V$, $c_{six'}/c_V$, $c_{eight'}/c_V$ = 1.10, 0.86, 0.76 (Table 4); the ratio is hardly affected when material properties are changed to E = 400 GPa and Γ = 1.048 MPa·m$^{1/2}$.

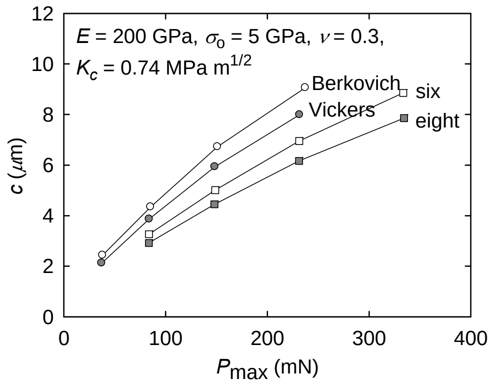

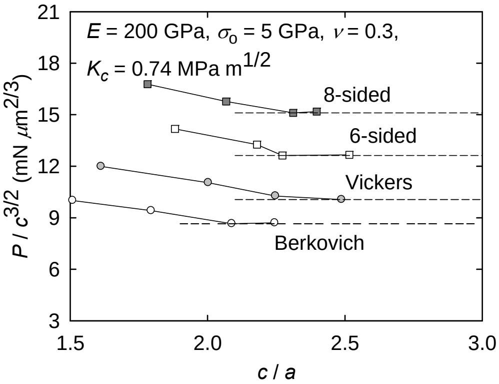

Figure 12. *left*: *c* vs. P_{max}, *right*: *c* / *a* vs. $P_{max} / c^{3/2}$ for 4 different ψ.

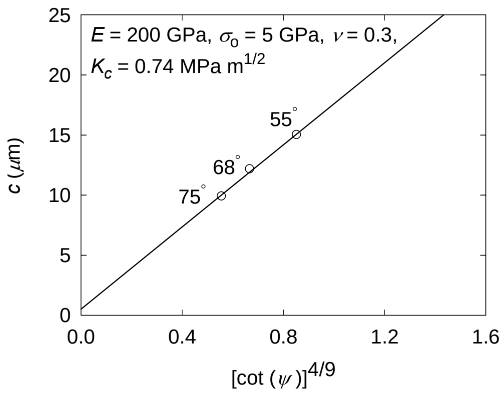

Figure 13 Variation of *c* with the centerline-to-face angle ψ.

Dukino and Swain (1992) compared the crack lengths for Berkovich and Vickers indentation on 6 different materials ($LinBO_3$, Ge, SF17, BK7, Si, SiC) and the crack length ratio c_B/c_V was found to be approximately 1.07 which is similar to our crack length ratio (1.10). Based on the crack length ratio, a formula is established expressing the relation between crack number n_c and crack length (normalized by c_V). Taking into account that c approaches zero for $n_c \rightarrow \infty$, we can write

$$c / c_V = k_1 e^{-k_2 n_c} \; ; \; (k_1, k_2) = (1.3680,\ 0.0778),\ n_c \geq 3 \tag{8}$$

By means of Equation 8, the crack length for other indenter shapes can be predicted based on the referential Vickers value. The corresponding graph is shown in Figure 11. For identical indenters (i.e. with equal n_c and ψ) one has to further study the change of c with ψ. Lawn et al. (Lawn, 1980) found α to be proportional to $(\cot\psi)^{2/3}$. Consequently, c is proportional to $(\cot\ \psi)^{4/9}$. This relation is in accordance with results from Vickers indentation cracking analysis (Figure 13).

Table 4. Comparison of crack lengths obtained from four different indenters.

***E* = 200 GPa, σ_{max} = 0.5 GPa, σ_o = 5 GPa, ν = 0.3, *f* = 0.2, δ_{max}/δ_c = 1/4**						
Cohesive zone properties	**P_{max} (mN)**	**c_V (μm)**	**c_B/c_V**	**c_V/c_V**	**c_{six}/c_V**	**c_{eight}/c_V**
K_c = 0.741 MPa·m$^{1/2}$ (*E* = 200GPa)	231.6	8.09	1.10	1.00	0.86	0.76
K_c = 1.048 MPa·m$^{1/2}$ (*E* = 400 Pa)	311.3	9.63	1.09	1.00	0.84	0.75

When c_1 is known for the angle ψ_1, c_2 can be obtained for a different angle ψ_2 through

$$c_2 = c_1 \left(\frac{\cot\psi_2}{\cot\psi_1} \right)^{4/9} \tag{9}$$

Eqations 8 and 9 provide a method to predict the crack length when an indenter of different geometry is employed (provided loads are equal). This means, any fracture toughness evaluation method for an indenter with a certain combination of (n_c, ψ) can be extended to indenters with different n_c and ψ.

5. Conclusion

Using FEA, we analyzed the change of crack length c with indenter shape (number of edges n_c and half-included angle ψ) for indentation cracking tests on brittle materials. To simulate indentation cracking in Abaqus, cohesive interfaces were placed in the radial planes where crack nucleation and propagation is expected. The behavior of the cohesive zones is governed by a simple traction-separation law. After comparing numerical analysis results with data from the literature, the FE model was found to be appropriate. To analyze crack characteristics for 3-sided pyramidal indentation (n_c = 3), indentation cracking tests on Si(100) and Ge(100) specimens were conducted with different loads and indenter angles. Hardness H and Young's modulus E were obtained from Berkovich indentation in an iterative manner by changing E in Abaqus until the FE load-indentation depth curve and E and H obtained by the O-P method were in a good agreement with experimental results. We then investigated the change of crack length c with the number of indenter edges n_c. Having confirmed that for equal indentation loads, c decreases when n_c is increased, an equation was established relating c (normalized by the reference Vickers crack length for the same load) to n_c. Similarly, keeping n_c constant, c was related to the half-included angle ψ. Applying these two equations, we can now predict from the crack length induced by one indenter the length of the crack that would be induced by an indenter of different geometry. This means that a fracture toughness evaluation method developed for one indenter type can be easily transformed into a more generalized form.

6. References

1. Abaqus User's Manual, Version 6.10, Dassault Systèmes Simulia Corp., Providence, RI, 2010.
2. Anstis, G.R., Chantikul, P., Lawn, B.R. and Marshall, D.B., "A Critical Evaluation of Indentation Techniques for Measuring Fracture Toughness: I, Direct Crack Measurements," Journal of the American Ceramic Society, Vol. 64, 1981.
3. Dukino, R.D. and Swain, M.V., "Comparative Measurement of Indentation Fracture Toughness with Berkovich and Vickers Indenters," Journal of the American Ceramic Society, Vol. 75, 1992.
4. Gao, Y.F. and Bower, A.F., "A Simple Techniques for Avoiding Convergence Problems in Finite Element Simulations of Crack Nucleation and Growth on Cohesive Interfaces," Modelling and Simulation in Materials Science and Engineering, Vol. 12, 2004.
5. Hill, R., "The mathematical theory of plasticity", Oxford University Press, Oxford, UK, 1950.
6. Hutchinson, J.W. and Evans, A.G., "Mechanics of Materials: Top-down Approaches to Fracture," *Acta Materialia*, Vol. 48, 2000.
7. Jang, J. and Pharr, G.M., "Influence of Indenter Angle on Cracking in Si and Ge During Nanoindentation," Acta Materialia, Vol. 56, 2008.
8. Jin, Z. and Sun C.T., "Cohesive Zone Modeling of Interface Fracture in Elastic Bi-materials," Engineering Fracture Mechanics, Vol. 72, 2005.
9. Laugier, M.T., "The Elastic/Plastic Indentation of Ceramics," Journal of Materials Science Letters, Vol. 4, 1985.
10. Lawn, B.R., Evans, A.G., and Marshall, D.B., "Elastic / Plasic Indentation Damage in Ceramics: the Median/Radial Crack System," Journal of the American Ceramic Society, Vol. 63, 1980.
11. Lee, J.H., Gao, Y., Johanns, K.E. and Pharr, G.M., "Cohesive Interface Simulations of Indentation Cracking as a Ftracture Toughness Measurement Method for Brittle Materials," Acta Materialia, Vol. 60, 2012.
12. Miyoshi, T., "A Study on Evaluation of K_{Ic} for Structural Ceramics," Transactions of the Japan Society of Mechanical Engineering, Vol. 51, 1985.
13. Niihara, K., "A Fracture Mechanics Analysis of Indentation-induced Palmqvist Cracks in Ceramics," Journal of Materials Science Letters, Vol. 2, 1983.

14. Oliver, W. C. and Pharr, G. M., “An Improved Technique for Determining Hardness and Elastic Modulus Using Load and Displacement Sensing Indentation Experiments,” Journal of Materials Research, Vol. 7, 1992.
15. Ouchterlony, F., “Stress Intensity Factors for the Expansion Loaded Star Crack,” Engineering Fracture Mechanics, Vol. 8, 1976.
16. Ponton, C.B. and Rawlings, R.D., “Vickers Indentation Fracture Toughness Test: Part 1. Review of Literature and Formulation of Standardised Indentation Equations,” Materials Science and Technology, Vol. 5, 1989a.
17. Ponton, C.B. and Rawlings, R.D., “Vickers Indentation Fracture Toughness Test: Part 2. Application and Critical Evaluation of Standardised Indentation Toughness Equations,” Materials Science and Technology, Vol. 5, 1989b.
18. Quin, G.D. and Bradt, R.C., “On the Vickers Indentation Fracture Toughness Test,” Journal of the American Ceramic Society, Vol. 90, 2007.
19. Shim, S., Oliver, W.C. and Pharr, G.M., “A Comparison of 3D Finite Element Simulation for Berkovich and Conical Indentation of Fused Silica,” International Journal of Surface Science and Engineering, Vol. 1, 2007.
20. Tang, Y., Yonezu, A., Ogasawara, N., Chiba, N. and Chen, X., “On Radial Crack and Half-penny Crack Induced by Vickers Indentation,” Proceedings of the Royal Society A, Vol. 464, 2008.
21. Williams, J.G., “Analytical Solutions for Cohesive Zone Models,” Journal of the Mechanics and Physics of Solids, Vol. 36, 2002.
22. Zhang, W. and Subhash, G., “Finite Element Aalysis of Iteractiong Vckers Identations on Bittle Materials,” Acta Materialia, Vol. 49, 2001.

7. Acknowledgements

This work was supported by the National Research Foundation grant funded by the Korean Ministry of Education, Science and Technology (MEST) (No. 2009-0083476).